

## Magnetic and microscopic characterization of magnetite nanoparticles adhered to clay surfaces

CECILIA GALINDO-GONZALEZ,<sup>1</sup> JOSHUA M. FEINBERG,<sup>2,\*</sup> TAKESHI KASAMA,<sup>3</sup>  
LIONEL CERVERA GONTARD,<sup>3</sup> MIHÁLY PÓSFAL,<sup>4</sup> ILONA KÓSA,<sup>4</sup> JUAN D.G. DURAN,<sup>1</sup>  
JAIME E. GIL,<sup>1</sup> RICHARD J. HARRISON,<sup>5</sup> AND RAFAL E. DUNIN-BORKOWSKI<sup>3</sup>

<sup>1</sup>Department of Applied Physics, Faculty of Sciences, University of Granada, C/Fuentenueva s/n, 18071 Granada, Spain

<sup>2</sup>Institute for Rock Magnetism, Department of Geology and Geophysics, University of Minnesota, Minneapolis, Minnesota 55455, U.S.A.

<sup>3</sup>Center for Electron Microscopy, Technical University of Denmark, DK-2800 Kongens Lyngby, Denmark

<sup>4</sup>Department of Earth and Environmental Sciences, University of Pannonia, POB 158, Veszprém H8200, Hungary

<sup>5</sup>Department of Earth Sciences, University of Cambridge, Downing Street, Cambridge CB2 3EQ, U.K.

### ABSTRACT

When suspended in solution, clay platelets coated with nanometer-scale magnetite particles behave as magnetorheologic fluids that are important to a variety of industrial applications. Such dual-phase assemblages are also similar to natural aggregates that record the direction and intensity of the Earth's magnetic field in lake and marine depositional environments. This study characterizes the mineralogical structure and magnetic behavior of montmorillonite platelets coated with aggregates of nanometer-scale magnetite crystals. The distribution of magnetite crystal sizes in three different clay-magnetite assemblages was directly measured using conventional transmission electron microscopy and agrees within error with estimates derived from magnetic hysteresis measurements. Magnetic hysteresis and low field susceptibility measurements combined with electron holography experiments indicate that all three samples behave superparamagnetically at room temperature, and show increasing levels of single domain behavior as the samples are cooled to liquid nitrogen temperatures. At such low temperatures, magnetostatic interactions are observed to partially stabilize otherwise superparamagnetic grains in flux closure structures.

**Keywords:** Magnetite, clay, smectite, TEM, electron holography, electron tomography, granulometry, magnetic properties

### INTRODUCTION

The behavior of magnetic particles in fluid environments is key to a multitude of industrial applications and plays an important role in the natural sciences. As small magnetic particles in lake and ocean waters settle out of the suspended sediment load, they adhere to the surfaces of clay platelets, and the resulting aggregates align themselves with respect to the Earth's magnetic field. Although this magnetic alignment can be influenced by various post-depositional processes, sediments act as permanent recorders of the Earth's magnetic field as they solidify into rock. In industrial applications, nanometer- and micrometer-scale magnetic particles are suspended in carrier fluids to create ferrofluids and magnetorheological fluids, which are frequently used as lubricants, dampening agents, heat conductors, optical refractometers, and medical delivery tools. It is possible to regulate the viscosity of these magnetic fluids by exposure to variable magnetic fields. The applied field causes suspended magnetic particles to align along lines of magnetic flux, thereby restricting movement of the carrier fluid. The use of suspended clay-magnetite aggregates, broadly analogous to those found in natural environments, amplifies this magnetorheologic effect

and is a recent advancement in the field of "smart fluids." The magnetic properties of these synthesized aggregates are determined by parameters such as the size, shape, and conformation of mineral grains within individual aggregate particles.

In the present study, we characterize a series of synthetic clay-magnetite assemblages comprehensively, with the aim of providing measurements that may shed light on the physical behavior of magnetorheological fluids as well as on the behavior of clay-magnetite aggregates in natural environments. Conventional transmission electron microscopy allows us to estimate the distribution of magnetite grain sizes and orientations in the aggregates. To obtain measurements of the three-dimensional shapes, positions, and orientations of nanometer-scale magnetite and clay particles we use a series of ultrahigh-tilt high-angle annular dark-field (HAADF) images to create three-dimensional electron tomographic reconstructions of individual aggregate particles. Off-axis electron holography, a TEM-based quantitative magnetic imaging technique, was used to study the magnetic microstructures of the clay-magnetite aggregates with nanometer-scale resolution. To put these nanometer-scale observations into the context of bulk sample behavior, we present measurements of temperature-dependent magnetic hysteresis and susceptibility.

\* E-mail: feinberg@umn.edu

## EXPERIMENTAL METHODS

### Sample preparation

Synthetic suspensions of clay-magnetite assemblages were created using the techniques described in Galindo-González et al. (2005). The clay mineral used in the assemblages is montmorillonite, which is smectite composed of tetrahedral (*t*) and octahedral (*o*) layers stacked in a *t-o-t* arrangement. The *t-o-t* layers in montmorillonite are negatively charged due to octahedral substitutions (e.g.,  $\text{Mg}^{2+}$  for  $\text{Al}^{3+}$  in the octahedral sheets). This negative charge attracts charge-balancing cations such as  $\text{Na}^+$  and  $\text{Ca}^{2+}$ , which bind the *t-o-t* layers together. The montmorillonite samples used in these experiments have been engineered so that  $\text{Na}^+$  is the only ion in the interlayer (Galindo-González et al. 2005, 2007). The magnetite particles in the clay-magnetite assemblages were synthesized by precipitation using the ferric and ferrous chloride technique of Massart (1981). The average grain size of particles produced using this technique is typically between 7 and 20 nm (Liu et al. 2004). The clay-magnetite assemblages were prepared by mixing suspensions of Na-montmorillonite and magnetite in proportion to obtain a desired magnetite/clay volume fraction ratio ( $\phi_m/\phi_c$ ). This study examined three samples with  $\phi_m/\phi_c$  ratios of 0.33, 1, and 3, which shall be referred to as samples 1:3, 1:1, and 3:1, respectively. The degree to which the magnetite grains adhere to the surface of the clay particles is controlled in part by the pH of the overall suspension (Tombácz et al. 2001), which was adjusted by the addition of NaOH or  $\text{HNO}_3$  solutions before and immediately after the mono-mineralic suspensions were mixed together. All samples were prepared using a pH value of  $\sim 3$ , where magnetite particles have positive surface charges and the clay particles have negative surface charges on basal planes. These conditions provide the highest probability for adhesion between the magnetite and montmorillonite particles, which in turn leads to the successful production of clay-magnetite assemblages.

### Electron microscopy

Conventional transmission electron microscopy was conducted at the Research Institute for Technical Physics and Materials Science, Budapest, Hungary, using a Philips CM20 TEM at 200 kV, where images and selected area electron diffraction (SAED) patterns were recorded on imaging plates. Off-axis electron holography was conducted at the University of Cambridge using a Philips CM300-ST field-emission-gun (FEG) TEM at 300 kV, where images were captured using a Gatan Imaging Filter (GIF). Ultrahigh-tilt series of HAADF images for electron tomography were obtained at the University of Cambridge at 200 kV using a FEI Tecnai F20 FEG TEM. HAADF images were acquired at  $2^\circ$  tilt intervals over a tilt range of  $-70$  to  $+74^\circ$  at a magnification of  $320,000\times$  and a camera length of 490 mm and used for three-dimensional tomographic reconstruction of the shapes of the magnetite and montmorillonite grains. The details of electron holography and electron tomography are well described by Dunin-Borkowski et al. (2004) and Weyland et al. (2006), respectively.

### Magnetic measurements

Magnetic susceptibility,  $\kappa$ , was measured as a function of temperature using an AGICO MFK1-FA Kappabridge instrument in the Department of Earth Sciences at the University of Cambridge. The instrument was operated using alternating fields ranging from 200 to 711 A/m and frequencies of 976, 3904, and 15 616 Hz. Sample masses were measured prior to each experiment to calculate mass-normalized susceptibility values. Samples were first cooled to  $-193^\circ\text{C}$  using liquid nitrogen and their magnetic susceptibility was measured during gradual warming back to room temperature. High-temperature magnetic susceptibility was measured as samples were heated to  $710^\circ\text{C}$ , either in argon or in air as indicated.

Hysteresis loops and first-order reversal curves (FORCs) were measured on a Princeton MicroMag 3900 vibrating sample magnetometer (VSM) in the Department of Material Sciences at the University of Cambridge. Samples were measured at room temperature and at  $-194^\circ\text{C}$ .

## RESULTS

### Conventional transmission electron microscopy

In all samples, the magnetite particles appear to cover the montmorillonite platelets in layers up to several crystals deep (Fig. 1). In the 1:3 sample the coverage is not continuous, whereas in the 3:1 sample the clay particles are entirely covered

by magnetite. Scattered magnetite crystals on the grid indicate that they detach fairly easily from the clay surface. The clay particles are thin and produce such weak contrast in bright-field (BF) images that in the 3:1 sample only the distinct shapes of the magnetite clusters suggest the presence of montmorillonite platelets.

The magnetite crystals have fairly uniform sizes as shown in Figure 2. Occasionally, erratic large magnetite crystals are found within the samples (see electron holography results below). At low magnification their shapes appear irregular and rounded, although at higher magnification facets are observed. Comparison of normal and log normal probability plots shows that crystal diameters are distributed log normally, which is consistent with previous TEM characterization studies on precipitated particles (Estournès et al. 1997; Belessi et al. 2008). The distribution of magnetite width/length ratios is relatively broad with a mean value near 0.82 (Fig. 3).

In past studies, nanometer-scale particles in solution have been observed to aggregate in crystallographic alignment with neighboring particles. This style of aggregation, termed “oriented aggregation,” has been observed in natural (Banfield et al. 2000) and synthetic (Penn and Banfield 1999; Privman et al. 1999) systems, and is highly dependent on solution chemistry (Penn et al. 2001). Because oriented aggregation can have important implications for a material’s subsequent reactivity, we examined the orientation relationships between the magnetite particles and the montmorillonite platelets.

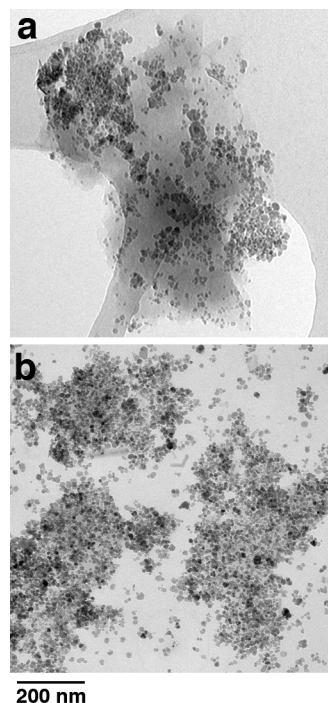


**FIGURE 1.** Bright-field TEM images of clay particles covered with magnetite crystals (a) sample 1:3 and (b) sample 3:1. In sample 3:1, magnetite crystals cover the montmorillonite platelets entirely, whereas the montmorillonite platelets in sample 1:3 are partially coated with magnetite crystals.

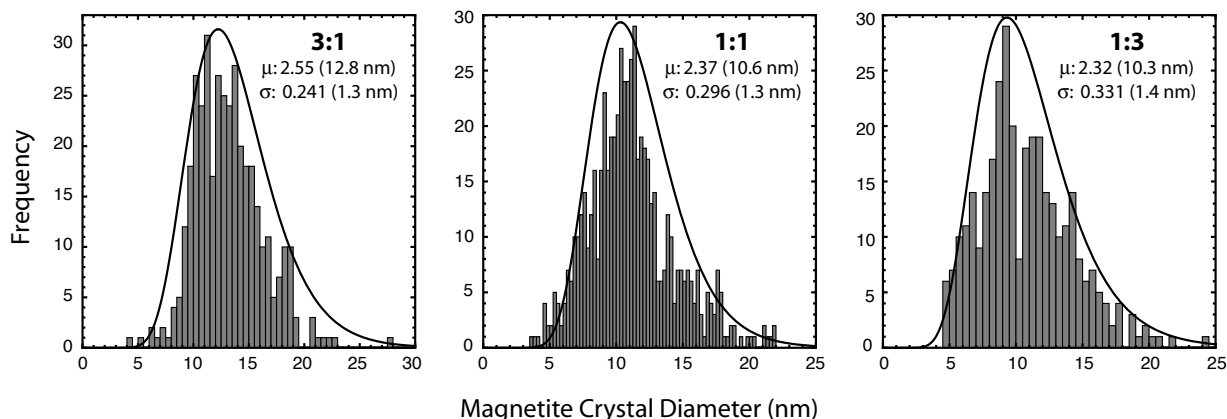


**FIGURE 2.** Size distributions of magnetite crystals in clay-magnetite assemblages. Measurements of crystal diameters were collected from TEM images and are plotted as histograms. Log normal distributions were generated from the mean ( $\mu$ ) and  $1\sigma$  values and are plotted as solid lines.

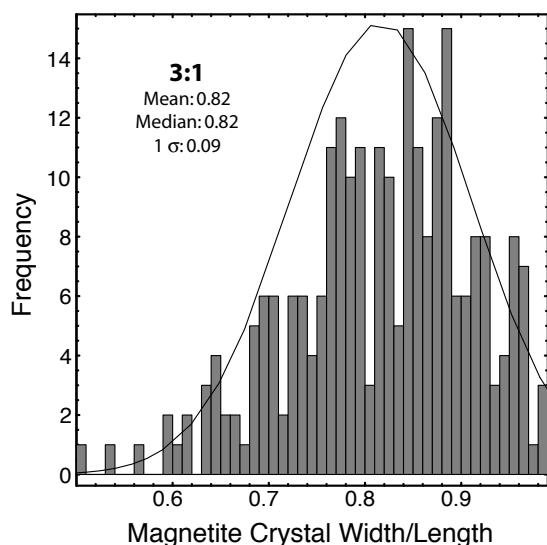


**FIGURE 3.** The distribution of magnetite crystal width/length ratios for the 3:1 sample. Mean elongation values fall near 0.82.

To test whether there is some shape-preferred orientation in the arrangement of elongated particles, we looked at the Fourier transform of several low-magnification images. The ring patterns observed in the Fourier transforms indicate that the orientation of magnetite elongations is completely random.

SAED patterns were obtained from several clay-magnetite assemblages. They all show rings that are consistent with the structure of magnetite (Fig. 4). In addition, there is a distinct 4.5 Å ring, which is characteristic of 110, 020 reflections of montmorillonite. The other reflections of montmorillonite will not be observed because the basal (001) plane lies flat on the TEM specimen grid. In short, the electron beam is almost parallel to the c-axis of montmorillonite.

To test whether a special orientation relationship exists between the clay platelets and magnetite particles, we analyzed the intensity distribution in SAED patterns in the 3:1 sample (Fig. 4). The intensities along each ring were integrated and plotted using software called Process Diffraction (Lábár 2005), and the resulting peaks were compared with a reference line profile of magnetite examined by powder X-ray diffraction. Apart from slight deviations, the intensity distributions of the

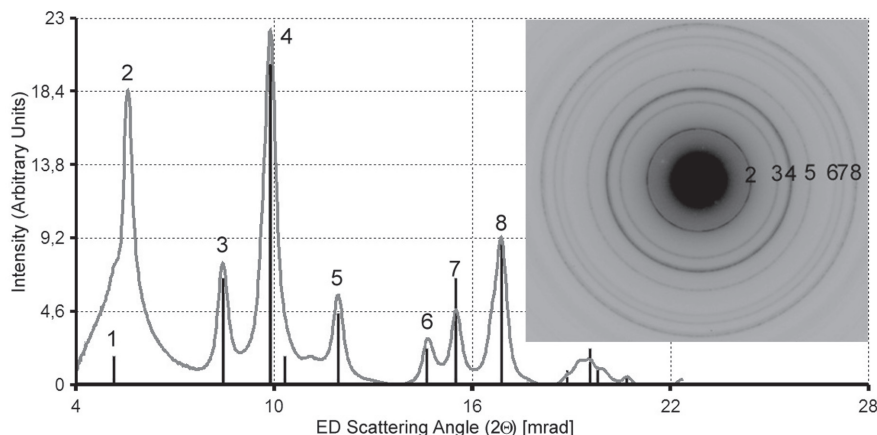


**FIGURE 4.** Background-subtracted intensity distribution, integrated along the diffraction circles of the inset SAED pattern that was obtained from a large cluster of clay-magnetite assemblages in the 3:1 sample. The strongly asymmetric left side of peak 2 is caused by imperfect background subtraction. Vertical lines indicate the X-ray powder diffraction intensities of magnetite. The numbers refer to the corresponding peaks in the SAED pattern. Peak 2 belongs to montmorillonite, whereas the other peaks belong to magnetite.

magnetite peaks are similar, suggesting that the existence of a preferred orientation between the magnetite crystals and the montmorillonite platelets is very unlikely. Thus, although we do not discount the possibility that oriented aggregation can occur in other clay-magnetite assemblages, the samples studied here show no such texture.

### Electron tomography

HAADF scanning transmission electron microscopy (STEM) tomography was used to determine the location, size, shape, and spacing of individual magnetite particles in three dimensions. The images were acquired using a Fischione Instruments 2020 single-tilt tomography holder in the tilt range of  $-70$  to  $+74^\circ$  with a tilt step of  $2^\circ$ . Alignment of the images and tomographic reconstruction using simultaneous iterative reconstruction techniques (SIRT) were performed using the software Inspect3D. Visualization of the final three-dimensional data sets was performed using Amira V2.3 software. After reconstruction, individual magnetite particles were examined in detail to obtain the Cartesian coordinates of their centers, as well as their corresponding diameters and volumes. (Such data are useful input for planned finite-element micromagnetic modeling of the assemblage.)

Figure 5 shows the reconstructed three-dimensional surface of a montmorillonite platelet surrounded by magnetite nanocrystals in the 3:1 sample. The magnetite particles are adhered mainly to the faces of the montmorillonite platelet. Magnetite grains are typically repelled from the edges of the clay platelet because the surface charge of both the magnetite particles and the edges of the clay platelet are positive at the acid pH used in this study (Hochella and Banfield 1995). Although the general morphology of the clay-magnetite assemblage can be seen in Figure 5, additional details can be observed in the supplemental<sup>1</sup> QuickTime movie. The tomographic images and movie also show magnetite nanocrystals accumulating in clusters several crystals in thickness on portions of the montmorillonite platelet. It is unclear whether these thick magnetite clusters formed prior to adhesion to the montmorillonite (while in mono-mineralic suspension) or whether they formed on a crystal-by-crystal basis after the two mono-mineralic suspensions were combined.

The particle size distribution obtained from the tomographic reconstruction is  $9.8 \pm 4.5$  nm, which agrees statistically with the distribution obtained from the conventional TEM images ( $13.2 \pm 3.2$  nm) for the same sample. We interpret the tomography-based mean to be a slight underestimate of the grain diameter for two reasons. HAADF images are more sensitive to particle's high Z regions, and consequently, low Z or disordered surface layers on the magnetite grains may not show up in these images, whereas they would appear in conventional bright-field images. Also the choice of isosurface contours used in the tomographic

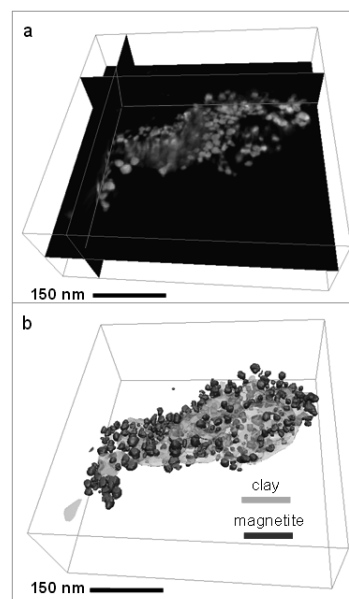


**FIGURE 5.** (a) Orthogonal sectioning of HAADF STEM tomographic reconstruction of a clay:magnetite assemblage in the 3:1 sample. (b) Visualization of the reconstructed volume shown in (a) showing the clay particle (light gray) surrounded by the magnetite particles (dark gray).

reconstruction is subjective, and is chosen to minimize streaking artifacts from the tomographic point spread function. This choice sometimes has the unintended effect of reducing the apparent particle size.

Using the data extracted from the tomographic reconstruction, the mean center-to-center distance between each particle and its neighbors was found to be 16.3 nm. The average number of neighboring particles found at this distance (the mean coordination number) is 6.33 and was determined using a probabilistic correlation function.

### Off-axis electron holography

Off-axis electron holography was used to examine the local magnetic properties of magnetite particle assemblages around individual montmorillonite platelets. Holograms of magnetic remanence for samples 3:1 and 1:3 were acquired using a liquid-nitrogen TEM specimen holder (approximately  $-181^\circ\text{C}$ ). Unwanted phase shift contributions due to the mean inner potential (thickness effect) were identified and eliminated using the technique of Kasama et al. (2006), where magnetic states of opposite sign were generated using the conventional objective lens in the TEM. The phase shift associated with the mean inner potential was isolated by summing two holograms of opposite magnetization. The resulting phase shift is equal to twice the mean inner potential contribution and can be digitally removed during image processing.

A magnetic induction map of magnetite particles adhered to a montmorillonite platelet in sample 1:3 is shown in Figure 6. The BF image (Fig. 6a) shows a fairly homogenous distribution of magnetite particles with two rare, anomalously large magnetite

<sup>1</sup> Deposit item AM-09-040, Supplemental QuickTime file (morphology of the clay-magnetite assemblage). This deposit item is only available electronically: at the MSA web site at <http://www.minsocam.org>. Or find it by going to the American Mineralogist Contents, find the table of contents for the specific volume/issue wanted, and then click on the deposit link there.



particles of diameter 47 and 48 nm. The two large particles touch each other and give a dipole-like magnetic signal (Fig. 6b). It is possible to use electron holograms to calculate the magnetic induction,  $B$ , of individual particles using the following equation for a uniformly magnetized sphere of radius  $a$ :

$$B = \frac{1}{2.044} \left( \frac{\hbar}{e} \right) \frac{\phi_{\text{MAG}}}{a^2}$$

where  $\phi_{\text{MAG}}$  is the phase shift in radians across the particle,  $\hbar$  is the reduced Planck's constant, and  $e$  is the electric charge. The magnetization of the particles is 0.53 T (420 kA m<sup>-1</sup>), which is consistent roughly with that expected for magnetite, 0.6 T (480 kA m<sup>-1</sup>). Such magnetic particles could be responsible for very small magnetization remanence measured in our bulk measurements at liquid nitrogen temperatures (see hysteresis results below). However, the assemblage of the smaller particles in the sample does not show any significant magnetic features (Fig. 6b), and the contours in this region could be artifacts due to image processing and are in the range of error. The two large particles showing a remanent magnetization are not common and most of the magnetite particles with sizes of <30 nm have no remanent signal. We interpret the particles that appear as non-magnetic to be superparamagnetic on the timescale required to collect an electron hologram (1 to 10 s). This interpretation is consis-

tent with the bulk magnetic measurements shown below. Five magnetite-montmorillonite assemblages from sample 3:1 were also investigated using electron holography at liquid nitrogen temperatures and no magnetic signals were observed.

Magnetic materials with uniaxial anisotropy such as elongated particles and nanoparticle-chains often display perfectly reversed magnetic remanent states when magnetized using equal and opposite fields (Figs. 7d and 7f). Occasionally agglomerates of magnetic particles do not exhibit this reversibility. Figure 7 shows an example of this non-reversibility. Two large crystals, with diameters of 37 and 43 nm, overlap one another and are positioned in the middle of an agglomerate. While the magnetic remanent structures in Figures 7c–7d and 7e–7f are similar but reversed, those in the Figures 7e–7f and 7g–7h are completely different from one another even though both were formed by the same field magnitude and direction. These different magnetic structures could be due to different relaxation processes related to the complex three-dimensional geometry of the aggregate (as opposed to the simpler geometries in chains or two-dimensional arrays). Similar nonreversible behavior has been observed in magnetite particle agglomerates in bacteria (Simpson, personal communication).

Stray fields from large particles often stabilize smaller magnetite particles in the agglomerate, which in isolation would be superparamagnetic. An example of such a feature is observed in Figures 7c–7d, where stray fields from the large particles return through small particles ~70 nm apart from the large particles. In Figures 7g–7h, the return fluxes of the large particles follow the distribution of magnetite nanoparticles. Thus, superparamagnetic-sized particles can be partially stabilized in flux closure geometry. Such structures may be one reason why these samples have little magnetic remanence (see hysteresis loop measurements). Flux closure structures and reduced magnetic remanence should be more prevalent in the 3:1 sample than in the 1:3 sample because the greater volume of magnetite promotes more three-dimensional agglomerates.

Figure 8 shows magnetic induction maps of two agglomerates, each of which contains two touching nanoparticles of different size. The particles in Figure 8a have diameters of 33 and 42 nm, whereas in Figure 8b the particles show diameters of 25 and 32 nm. The assemblage containing the larger particles clearly shows a magnetic signal (Fig. 8c), whereas the assemblage with the smaller particles appears to be non-magnetic (Fig. 8d). This difference provides a rough estimate of 30–40 nm for the critical size threshold for superparamagnetic behavior in three-dimensional assemblages, which suggests that most of the magnetite particles in the samples in this study should be superparamagnetic on timescales of ~10 s (the time needed for hologram collection). Based on a larger set of experimental observations, Simpson (personal communication) finds an empirical threshold size of 20–25 nm for superparamagnetic behavior in two-dimensional arrays of magnetite particles. Although this value is smaller than our estimate, it is possible that two- and three-dimensional particle assemblages would have different threshold values for superparamagnetic behavior. An alternative explanation for the slight difference in our estimates may be that the synthetic magnetite used in this study was damaged or partially oxidized during sample preparation.

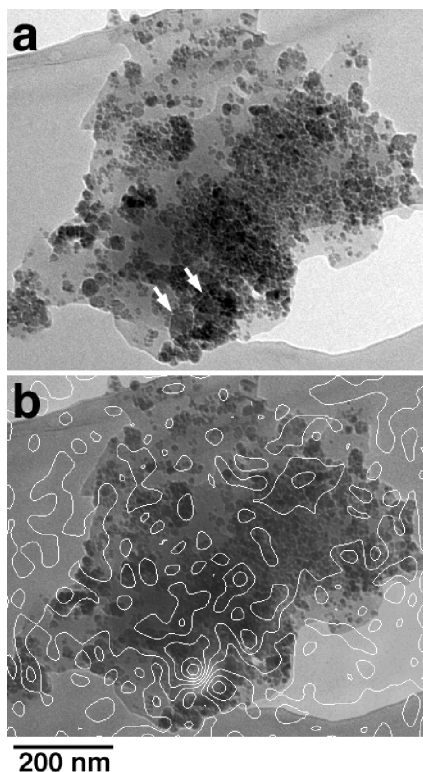


**FIGURE 6.** (a) Bright-field TEM image of magnetite particles adhering to a montmorillonite grain in the 1:3 sample and (b) the corresponding magnetic remanence contour map acquired at  $-181^{\circ}\text{C}$ . There are two large crystals, 47 nm in diameter for the left and 48 nm for the right, shown with the arrow in a. The phase contour spacing is 0.125 radians.

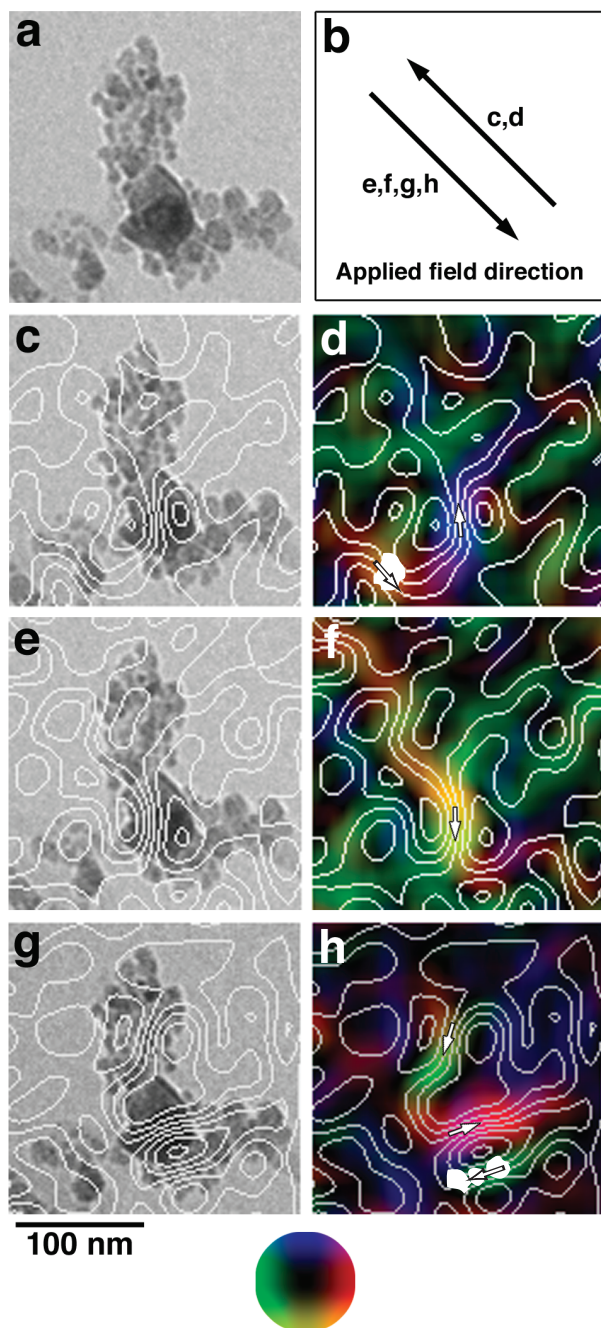


**FIGURE 7.** (a) BF image of two large crystals within an agglomerate of smaller crystals in the 1:3 sample. (b) Applied field directions in the following images, c–h. (c and d) Magnetic contour and induction color maps at remanence when saturated in the NW direction. (e–h) Magnetic contour and induction color maps at remanence when saturated in the SE direction with a field of 2 T. Note that e, f and g, h have different remanent structures even after the same field was applied. The local magnetic direction is shown with arrows in d, f, and h. Superparamagnetic-sized grains whose magnetizations are stabilized by return flux from nearby larger magnetite grains are outlined in white in d and h. The phase contour spacing is 0.0625 radians. The direction of measured magnetic induction is shown according to a color wheel (red = right, yellow = down, green = left, blue = up).

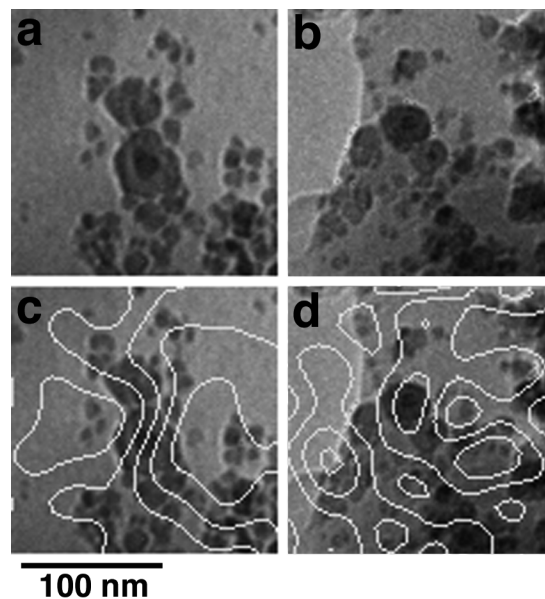


**FIGURE 8.** BF images of assemblages in sample 1:3 containing two large, touching particles within an assortment of smaller particles (a and b) and their corresponding magnetic induction maps (c and d). The large particles in a and c have diameters of 33 and 42 nm, whereas those in b and d have diameters of 25 and 32 nm. The phase contour spacing is 0.0625 radians.

#### Magnetic susceptibility

Due to the large quantity of magnetite in the magnetite:clay assemblages, the susceptibility signal for all three samples was far above the background sensitivity of the susceptibility meter. Mass-normalized room temperature susceptibilities ranged from  $4 \times 10^{-4}$  to  $1.1 \times 10^{-3}$  m<sup>3</sup>/kg, which are several orders of magnitude larger than previously measured values for the mass normalized susceptibility of montmorillonite ( $1.4 \times 10^{-7}$  m<sup>3</sup>/kg) (Dunlop and Özdemir 1997).

The susceptibility of each sample is shown as a function of temperature in Figure 9. During heating, the susceptibility increases toward a broad peak and then gradually decreases to zero near the Curie temperature of pure magnetite (580 °C). The shapes of these curves are consistent with superparamagnetic behavior, where the peak susceptibility corresponds to the average superparamagnetic blocking temperature of the magnetite grains in the sample. Below the blocking temperature, anisotropy energy is greater than thermal energy and the magnetite grains begin behaving as an assemblage of interacting single domain particles. The change in magnetic domain state causes the susceptibility to decrease because single domain grains are less susceptible to alignment in small magnetic fields. As the temperature continues to decrease, more magnetite particles pass through their blocking temperatures, and the susceptibility continues to decrease further. Above the superparamagnetic blocking temperature, thermal energy causes a progressive decline in magnetite's saturation magnetization, which in turn decreases the overall strength of the sample's susceptibility. Similar superparamagnetic susceptibility behavior was observed in particle assemblages of lithium ferrite (Verma and Joy 2005).

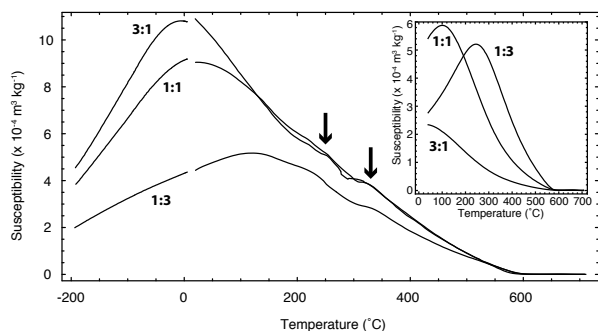


**FIGURE 9.** Mass-normalized in-phase susceptibility as a function of temperature for the magnetite-coated clay samples. Experiments were conducted in argon using an AC field of  $200 \text{ A m}^{-1}$  and a frequency of  $976 \text{ Hz}$ . The curves indicate superparamagnetic behavior in all three samples. None of the samples display a clear Verwey transition or Curie temperature. The perturbations at  $250$  and  $330^\circ\text{C}$  (arrows) are related to dewatering of the montmorillonite. Inset shows the cooling curves for the same samples. The peak susceptibility temperatures in samples 1:1 and 3:1 have increased, indicating thermal coarsening.

The slight perturbations in the susceptibility at  $\sim 250$  and  $\sim 330^\circ\text{C}$  are related to the dehydration of the montmorillonite. Water molecules between the silicate sheets in montmorillonite are typically driven off between  $20$  and  $200^\circ\text{C}$  (Balek et al. 2006). Although all experiments were conducted in an argon atmosphere, the liberation of water vapor during the experiment allowed minor oxidation and surface modification of the samples to form maghemite ( $\gamma\text{-Fe}_2\text{O}_3$ ) and/or hematite ( $\alpha\text{-Fe}_2\text{O}_3$ ). The effects of this oxidation were most apparent on cooling the samples back to room temperature, where we observe an 80% difference between the pre- and post-heating susceptibility. When experiments were conducted in air, a new susceptibility peak appears at  $660^\circ\text{C}$ , which we attribute to hematite.

Although the magnetic susceptibility curves indicate increased single domain behavior for all samples at liquid nitrogen temperatures, it is important to consider the large frequency of the field used in these experiments. At a frequency of  $976 \text{ Hz}$ , a crystal with a relaxation time of just over  $2 \times 10^{-3} \text{ s}$  would appear as single domain. In contrast, electron holograms are typically collected over a timescale of  $1$  to  $10 \text{ s}$ . Figures 6–8 show that only the largest grains have relaxation times at this scale at liquid nitrogen temperatures.

### Hysteresis measurements

Room-temperature hysteresis loops for all three synthetic samples display classic superparamagnetic behavior and are shown in Figure 10. The loops are perfectly reversible and show no magnetic remanence at room temperature. When hysteresis loops are measured at  $-194^\circ\text{C}$  (Fig. 11), portions of the magnetite grains have passed through their superparamagnetic blocking temperatures and behave as single domain grains. All three samples display magnetic remanence at  $-194^\circ\text{C}$ .

To examine the coercivity distribution in the samples at low temperature, first-order reversal curves (FORCs) were measured, and a representative FORC diagram is shown in Figure 12. The diagram shows that portions of the sample are behaving as single domain grains with coercivities ranging from  $\sim 2.5$  to  $25 \text{ mT}$ . A

fraction of the sample is still behaving superparamagnetically as suggested by the portion of the FORC distribution that extends along the  $H_u$  axis near the origin.

## DISCUSSION

### Modeling magnetic behavior

The average grain size of the magnetite particles adhering to the montmorillonite flakes can be estimated by fitting Langevin functions to the hysteresis data. A Langevin function has the form  $L(\alpha) = \coth(\alpha) - \alpha^{-1}$ , where  $\alpha = \mu_0 V M_s H / kT$ .  $\mu_0$  is the permeability of free space,  $V$  is volume of a grain,  $M_s$  is the saturation magnetization of the grain,  $H$  is the applied field,  $k$  is the Boltzmann constant, and  $T$  is the temperature. Langevin functions have been used in previous studies to model paramagnetic and superparamagnetic materials (e.g., Tauxe et al. 1996; Dunlop and Özdemir 1997; Worm and Jackson 1999). This technique is also only applicable when  $KV/kT \ll 1$ , as is the case for our samples at room temperature, where  $K$  is magnetic anisotropy constant.

When the magnetization data for the magnetite-montmorillonite samples is compared to Langevin curves calculated for a series of different spherical particles (Fig. 13), we see that it is difficult to estimate the grain size using a single curve. At low and high applied fields, the magnetite-montmorillonite samples appear to match the Langevin curves for  $15\text{--}20 \text{ nm}$  particles, whereas at intermediate applied fields ( $20\text{--}100 \text{ mT}$ ) the samples match the Langevin curves for  $10 \text{ nm}$  particles. The reason for this poor fit is likely a result of trying to fit the magnetic behavior of a distribution of different particles sizes with a function for a single particle size. Additionally, Langevin curves are insensitive to the inter-particle spacing in an assemblage of grains.

The hysteresis data can be successfully modeled if the Langevin curves for a distribution of grain sizes are summed to produce a cumulative curve (Fig. 14). We estimated the grain size distribution in our samples by fitting cumulative Langevin curves generated by log normal distributions of spherical magnetite nanocrystals to the room-temperature hysteresis data. As noted by Scherbakov and Fabian (2005), it is exceedingly difficult to unambiguously determine the grain size distribution of superparamagnetic assemblages from high- or low-field susceptibility data without making significant assumptions about the nature of the grain size distribution (e.g., Gaussian or log-normal), the inferred shape of the grains, and the arrangement of crystallographic easy axes. Based on observations from conventional TEM images (Fig. 2) and crystal orientations observed in SAED patterns, we assume a log normal grain size distribution of randomly oriented particles in each sample. The resulting magnetically derived distributions agree well with the independently determined distributions from conventional TEM images.

### Magnetostatic interactions

The close proximity of magnetite particles on the surface of the clay platelets implies that magnetostatic interactions will play a significant role in controlling the magnetic properties of these samples. There are two important consequences of magnetostatic interactions in the current context. At high temperatures, all particles are well above their blocking temperature and behave



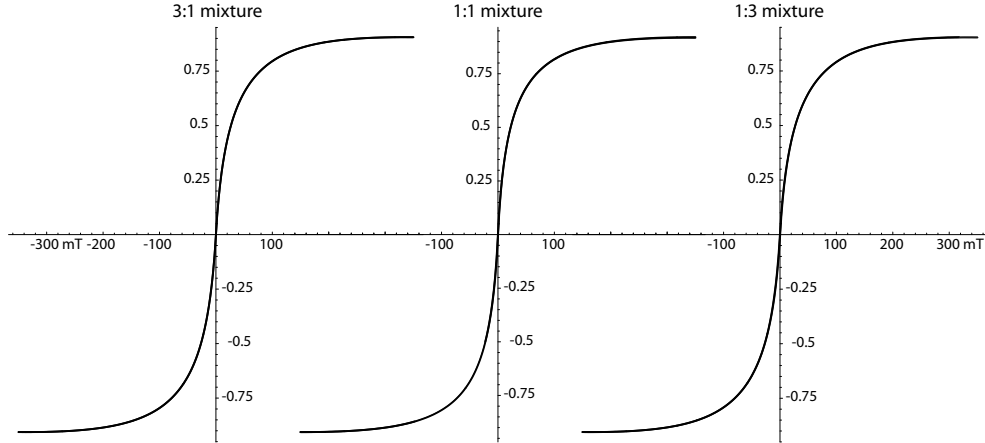


**FIGURE 10.** Normalized hysteresis loops of the magnetite-montmorillonite mixtures. Both the ascending and descending portions of the hysteresis loops are plotted. The two curves completely overlap.

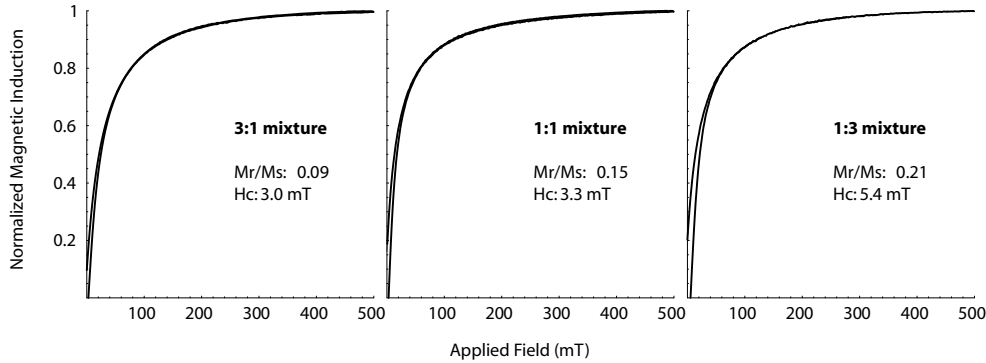


**FIGURE 11.** Normalized hysteresis loops collected at  $-194^{\circ}\text{C}$ . All three magnetite:clay mixtures display magnetic remanence at these temperatures.

superparamagnetically. An assemblage of non-interacting, randomly oriented superparamagnetic particles has an isotropic magnetic susceptibility. The use of these particles in magnetorheologic fluids requires that the clay particles orient themselves with respect to an applied magnetic field, which, in turn, requires that the superparamagnetic susceptibility be anisotropic. This anisotropy can be explained by the dipole-dipole interactions between particles distributed across the surfaces of the clay platelets, in the same way that dipole-dipole interactions between atomic spins lead to the shape anisotropy of an individual oblate spheroidal particle. The susceptibility of the clay particles will be significantly higher for magnetic fields applied parallel to the platelet surfaces than for fields applied normal to the surfaces, causing the platelets to rotate into alignment. The second important consequence is that the overall susceptibility is lowered by dipole-dipole interactions.

Magnetostatic interactions within assemblages of superparamagnetic grains are known to cause uncertainties in estimates of magnetic grain size distributions (Fiorani et al. 1999; Scherbakov and Fabian 2005). Past studies have generally used one of two general approaches to modeling the role of magnetostatic interac-

tions between superparamagnetic grains: utilizing mean interaction fields (e.g., Scherbakov and Fabian 2005) or energy barriers for individual grains (e.g., Dormann et al. 1997). Scherbakov and Fabian (2005), used mean interaction fields to describe the role of magnetostatic interactions on the complex susceptibility,  $\chi(\omega, \tau)$ , of superparamagnetic assemblages:

$$(\omega, \tau) = \frac{\chi_0 \langle \sec h^2 [\beta V h_{int}] \rangle}{1 + i\omega\tau}$$

where  $\omega$  is the frequency of an AC magnetic field,  $\tau$  is the relaxation time,  $\chi_0$  is the static initial susceptibility,

$$\beta = \frac{\mu_0 M_s [T] H_k [T]}{kT}$$

$M_s [T]$  and  $H_k [T]$  are the saturation magnetization and microcoercivity as a function of temperature, respectively, and  $h_{int}$  is the mean interaction field,  $H_{int}$ , normalized by the microcoercivity. These relationships are useful because they call attention to two trends: (1) the role of interactions will increase as temperature drops, and (2) at constant temperatures, the role of interactions will increase as a function of grain volume. Larger interactions



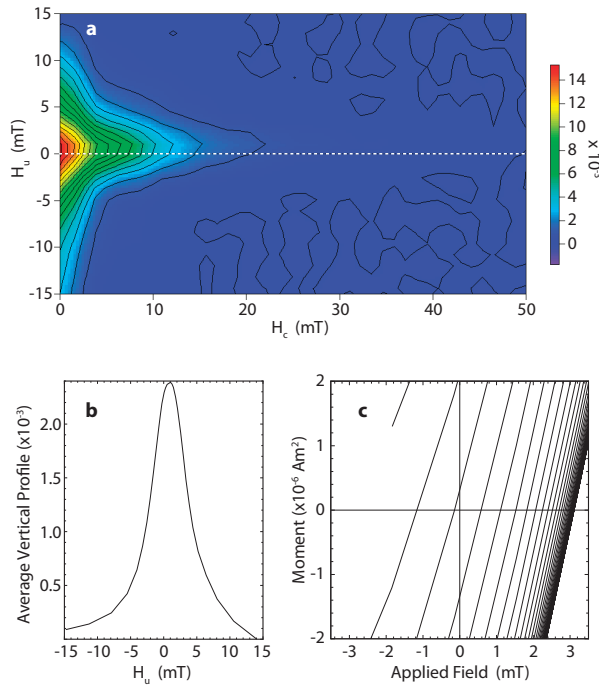


**FIGURE 12.** (a) First-order reversal curve diagram for the 3:1 magnetite:montmorillonite sample collected at  $-194^{\circ}\text{C}$ . Most of the grains in the sample are behaving superparamagnetically, as indicated by the coercivities near the origin extending along the  $H_u$  axis. However, the distribution of higher coercivity values that extends along the  $H_u = 0$  line indicates that a portion of the assemblage has begun to behave as single-domain grains.  $\text{SF} = 2.2$ . (b) The average vertical profile of the FORC diagram shows a +1 mT asymmetric peak shift. (c) A close-up of the FORCs near the origin. Produced using FORCinel (Harrison and Feinberg 2008).

fields are thought to stabilize the magnetization of a superparamagnetic assemblage, and thereby reduce the susceptibility of the assemblage (Fiorani et al. 1999).

Magnetostatic interactions played a significant role in our observations of the magnetite-montmorillonite assemblages even at liquid nitrogen temperatures. The largest magnetite crystals passed through their blocking temperature and began behaving as single domain grains. The magnetostatic fields generated by

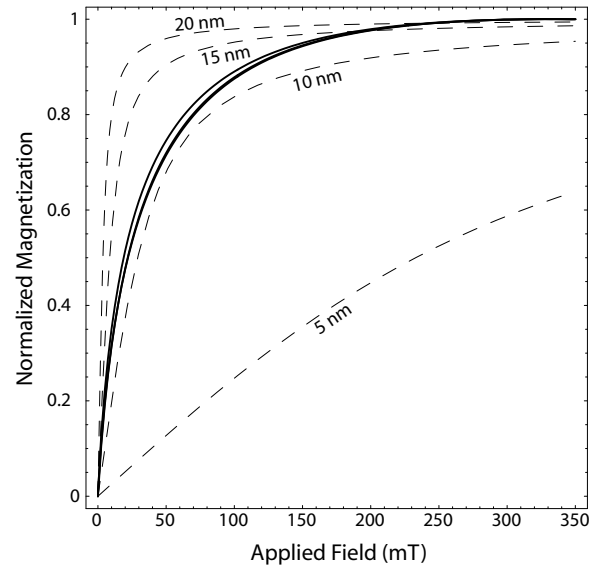


**FIGURE 13.** Normalized magnetization curves (solid lines) for all three magnetite-montmorillonite samples at room temperature (295 K), together with Langevin curves calculated for particle diameters of 5, 10, 15, and 20 nm.

such large grains are stable and are able to partially stabilize the moments of smaller neighboring grains in flux closure structures (Fig. 7). FORC diagrams collected at liquid nitrogen temperatures show interaction fields up to  $\pm 5$  mT around the  $H_u = 0$  axis. When the average vertical profile for the FORC diagram in Figure 12 is calculated (Fig. 12b), we observe a positive 1 mT peak shift away from the  $H_u = 0$  axis. Although the vertical asymmetry of the FORC diagram is small, the magnitude and sign of the shift are consistent with a mean interaction field associated with the flux closure structures observed in the low-temperature electron holography images (Fig. 8). A shift of 1 mT is also consistent with the 1–2 mT mean interaction fields estimated for ferrofluids by Scherbokov and Fabian (2005). At even lower temperatures, where a larger percentage of the magnetite will behave as stable single domain particles, the magnitude of the interactions will continue to increase and more complex vortex-like magnetic microstructures will begin to form, similar to those observed in Harrison et al. (2002) and Feinberg et al. (2006).

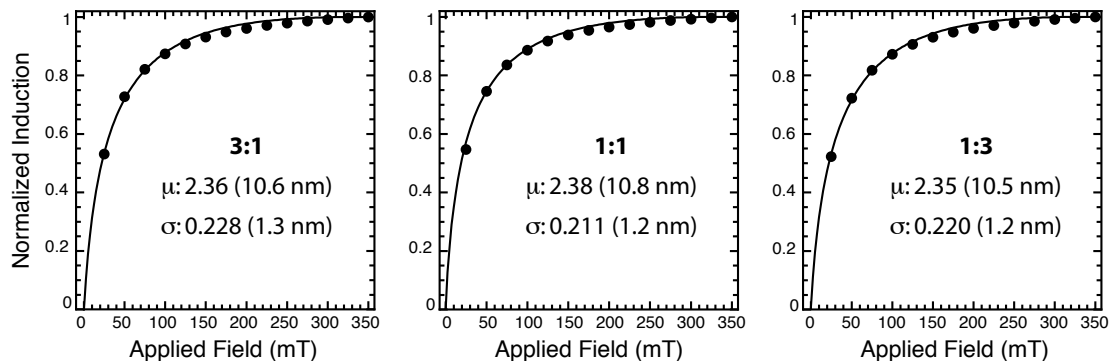


**FIGURE 14.** Modeled hysteresis behavior using normal grain size distributions. Black lines show measured hysteresis data. Circles show the predicted hysteresis behavior using the indicated log normal distribution of grain diameters.

## CONCLUDING REMARKS

The grain size distribution and random crystallographic orientation of magnetite nanocrystals in these synthetic samples guarantee superparamagnetic behavior at room temperature. Such behavior is ideal for magnetorheologic fluids, which need to respond quickly to changes in applied field. At progressively lower temperatures, the relaxation time of the magnetite grains begins to increase, and the magnetic response time of the magnetorheologic fluid will dampen.

The samples studied here are broadly similar to the clay-magnetite assemblages that occur in marine and lacustrine environments. Naturally occurring clay-magnetite assemblages typically have larger grain size distributions that are dominated by single domain behavior at ambient temperatures. In the synthetic samples studied here, the planar assemblages of superparamagnetic grains around montmorillonite platelets create an inherent anisotropic susceptibility. This anisotropy allows an assemblage to align itself with a magnetizing field in industrial applications and may potentially allow such assemblages to align themselves in the presence of the Earth's magnetic field. Similar assemblages of interacting superparamagnetic grains have been observed in natural settings in previous studies (Lovely et al. 1987; Sparks et al. 1990; Franke et al. 2007). Although these superparamagnetic assemblages would be incapable of retaining a magnetic remanence, it may be possible to recover a recording of the Earth's ancient magnetic field direction in sediments containing a high proportion of such assemblages by measuring a sample's anisotropy of magnetic susceptibility (AMS) tensor.

## ACKNOWLEDGMENTS

J.M.F. received support from the Natural Environment Research Council grant NE/C518422/1. T.K. and R.D.B. received support from NERC grant NE/D002036/1. M.P. received support from the Hungarian Science Fund (OTKA 48607). We thank L. Tauxe and D. Bilardello for thoughtful reviews that greatly improved the manuscript.

## REFERENCES CITED

- Balek, V., Benes, M., Málek, Z., Matuschek, G., Ketrup, A., and Yariv, S. (2006) Emanation thermal analysis study of Na-montmorillonite and montmorillonite saturated with various cations. *Journal of Thermal Analysis and Calorimetry*, 3, 617–623.
- Banfield, J.F., Welch, S.A., Zhang, H., Ebert, T.T., and Penn, R.L. (2000) Aggregation-based crystal growth and microstructure development in natural iron oxyhydroxide biomineralization products. *Science*, 289, 751–754.
- Belessi, V., Zboril, R., Tucek, J., Mashlan, M., Tzitzios, V., and Petridis, D. (2008) Ferrofluids from magnetic-chitosan hybrids. *Chemistry of Materials*, 20, 3298–3305.
- Dormann, J.L., Fiorani, D., and Tronc, E. (1997) Magnetic relaxation in fine-particle systems. *Advances in Chemical Physics*, 98, 283–494.
- Dunin-Borkowski, R.E., McCartney, M.R., and Smith, D.J. (2004) Electron holography of nanostructured materials. In H.S. Nalwa, Ed., *Encyclopedia of Nanoscience and Nanotechnology*, 3, 41–100. American Scientific Publishers, Stevenson Ranch, California.
- Dunlop, D.J. and Özdemir, Ö. (1997) *Rock Magnetism: Fundamentals and Frontiers*, 573 p. Cambridge University Press, U.K.
- Estournès, C., Lutz, T., Hapich, J., Quaranta, T., Wissler, P., and Guille, J.L. (1997) Nickel nanoparticles in silica gel: preparation and magnetic properties. *Journal of Magnetism and Magnetic Materials*, 173, 83–92.
- Feinberg, J.M., Harrison, R.J., Dunin-Borkowski, R.E., Kasama, T., Scott, G.R., and Renne, P.R. (2006) Effects of internal mineral structures on the magnetic remanence of silicate-hosted titanomagnetite inclusions: An electron holography study. *Journal of Geophysical Research: Solid Earth*, 111, B12S15, DOI: 10.1029/2006JB004498.
- Fiorani, D., Dormann, J.L., Cherkaoui, R., Tronc, E., Lucari, F., D'Orazio, F., Spinu, L., Nogués, M., García, A., and Testa, A.M. (1999) Collective magnetic state in nanoparticle systems. *Journal of Magnetism and Magnetic Materials*, 196, 143–147.
- Franke, C., von Dobeneck, T., Drury, M.R., Meeldijk, J.D., and Dekkers, M.J. (2007) Magnetic petrology of equatorial Atlantic sediments: Electron microscopy results and their implications for environmental magnetic interpretation. *Paleoceanography*, 22, PA4207, DOI: 10.1029/2007PA001442.
- Galindo-González, C., de Vicente, J., Ramos-Tejada, M.M., López-López, M.T., González-Caballero, F., and Durán, J.D.G. (2005) Preparation and sedimentation behavior in magnetic fields of magnetite-covered clay particles. *Langmuir*, 21, 4410–4419.
- Galindo-González, C., Iglesias, G.R., González-Caballero, F., and Durán, J.D.G. (2007) Stability of concentrated aqueous clay-magnetite suspensions. *Colloids and Surfaces A: Physicochemical and Engineering Aspects*, 306, 150–157, DOI: 10.1016/j.colsurfa.2006.12.076.
- Harrison, R.J. and Feinberg, J.M. (2008) FORCinel: An improved algorithm for calculating first-order reversal curve (FORC) distributions using locally-weighted regression smoothing. *Geochemistry, Geophysics, Geosystems*, 9, Q05016, DOI: 10.1029/2008GC001987.
- Harrison, R.J., Dunin-Borkowski, R.E., and Putnis, A. (2002) Direct imaging of nanoscale magnetic interactions in minerals. *Proceedings of the National Academy of Sciences of the United States of America*, 99, 16556–16561.
- Hochella Jr., M.F. and Banfield, J.F. (1995) Chemical weathering of silicates in nature: A microscopic perspective with theoretical considerations. In A.F. White and S.L. Brantley, Eds., *Chemical Weathering Rates of Silicate Minerals*, 31, p. 353–406. Reviews in Mineralogy and Geochemistry, Mineralogical Society of America and Geochemical Society, Chantilly, Virginia.
- Kasama, T., Pösfai, M., Chong, R.K.K., Finlayson, A.P., Buseck, P.R., Frankel, R.B., and Dunin-Borkowski, R.E. (2006) Magnetic properties, microstructure, composition, and morphology of greigite nanocrystals in magnetotactic bacteria from electron holography and tomography. *American Mineralogist*, 91, 1216–1229.
- Lábár, J.L. (2005) Consistent indexing of a (set of) single crystal SAED pattern(s) with the ProcessDiffraction program. *Ultramicroscopy*, 103, 237–249.
- Liu, Z.L., Wang, H.B., Lu, Q.H., Du, G.H., Peng, L., Du, Y.Q., Zhang, S.M., and Yao, K.L. (2004) Synthesis and characterization of ultrafine well-dispersed magnetic nanoparticles. *Journal of Magnetism and Magnetic Materials*, 283, 258–262.
- Lovely, D.R., Stolz, J.F., Nord, G.L., and Phillips, E.J.P. (1987) Anaerobic production of magnetite by a dissimilatory iron-reducing microorganism. *Nature*, 330, 252–254.
- Massart, R. (1981) Preparation of aqueous magnetic liquids in alkaline and acidic media. *IEEE Transactions on Magnetics*, 17, 1247–1248.
- Penn, R.L. and Banfield, J.F. (1999) Morphology development and crystal growth in nanocrystalline aggregates under hydrothermal conditions: Insights from titanite. *Geochimica et Cosmochimica Acta*, 63, 1549–1557.
- Penn, R.L., Oskam, G., Strathmann, T.J., Searson, P.C., Stone, A.T., and Veblen, D.R. (2001) Epitaxial assembly in aged colloids. *Journal of Physical Chemistry B*, 105, 2177–2182.
- Privman, V., Goia, D.V., Park, J., and Matijevic, E. (1999) Mechanism of formation of monodispersed colloids by aggregation of nanosize precursors. *Journal of Colloid and Interface Science*, 231, 36–45.
- Scherbakov, V.P. and Fabian, K. (2005) On the determination of magnetic grain-size distributions of superparamagnetic particle ensembles using frequency dependence of susceptibility at different temperatures. *Geophysical Journal International*, 162, 736–746.
- Sparks, N.H.C., Mann, S., Bazylinski, D.A., Lovely, D.R., Jannasch, H.W., and Frankel, R.B. (1990) Structure and morphology of magnetite anaerobically-produced by a marine magnetotactic bacterium and a dissimilatory iron-reducing bacterium. *Earth and Planetary Science Letters*, 98, 14–22.
- Tauxe, L., Mullender, T.A., and Pick, T. (1996) Potbellies, wasp-waists, and superparamagnetism in magnetic hysteresis. *Journal of Geophysical Research*, 101, 571–583.
- Tombácz, E., Csanaky, C., and Illés, E. (2001) Polydisperse fractal aggregate formation in clay mineral and iron oxide suspensions, pH, and ionic strength dependence. *Colloid and Polymer Science*, 279, 484–492.
- Verma, S. and Joy, P.A. (2005) Magnetic properties of superparamagnetic lithium ferrite nanoparticles. *Journal of Applied Physics*, 98, 124312.
- Weyland, M., Yates, T.J.V., Dunin-Borkowski, R.E., Laffont, L., and Midgley, P.A. (2006) Nanoscale analysis of three-dimensional structures by electron tomography. *Scripta Materialia*, 55, 29–33.
- Worm, H.-U. and Jackson, M. (1999) The superparamagnetism of Yucca Mountain Tuff. *Journal of Geophysical Research*, 104, 25415–25425.